Wind and Structures, *Vol. 20, No. 1 (2015) 75-93*
DOI: http://dx.doi.org/10.12989/was.2015.20.1.075

Parametric numerical study of wind barrier shelter

Marijo Telenta[*1], Milan Batista[2], M.E. Biancolini[3], Ivan Prebil[1] and Jožef Duhovnik[1]

[1]*Faculty of Mechanical Engineering, University of Ljubljana, Aškerčeva 6, 1000 Ljubljana, Slovenia*
[2]*Faculty of Maritime studies and Transport, University of Ljubljana, Pot pomorščakov, 6320 Portorož, Slovenia*
[3]*Department of Enterprise Engineering, University of Rome "Tor Vergata", Via Politecnico 1, 00133 Roma, Italy*

(Received July 24, 2014, Revised November 21, 2014, Accepted November 29, 2014)

Abstract. This work is focused on a parametric numerical study of the barrier's bar inclination shelter effect in crosswind scenario. The parametric study combines mesh morphing and design of experiments in automated manner. Radial Basis Functions (RBF) method is used for mesh morphing and Ansys Workbench is used as an automation platform. Wind barrier consists of five bars where each bar angle is parameterized. Design points are defined using the design of experiments (DOE) technique to accurately represent the entire design space. Three-dimensional RANS numerical simulation was utilized with commercial software Ansys Fluent 14.5. In addition to the numerical study, experimental measurement of the aerodynamic forces acting on a vehicle is performed in order to define the critical wind disturbance scenario. The wind barrier optimization method combines morphing, an advanced CFD solver, high performance computing, and process automaters. The goal is to present a parametric aerodynamic simulation methodology for the wind barrier shelter that integrates accuracy and an extended design space in an automated manner. In addition, goal driven optimization is conducted for the most influential parameters for the wind barrier shelter.

Keywords: parametric numerical simulation; wind barrier shelter; RBF morph; CFD simulation; mesh morphing

1. Introduction

Wind barriers are the earliest devices used to control wind flow. They are utilized in numerous shelter applications to improve windy conditions that would be appropriate for human needs. For many years, wind barriers have been employed to prevent strong wind effects in secluded areas. In particular, wind barriers can offer optimal protection if used correctly and efficiently. They have been studied since the 1940s in order to find optimum shelter protection. The basic purpose of the wind barrier is to reduce the wind velocity within a certain distance. There are two main types of wind barriers: solid and porous. Primarily porous wind barriers are exploited as turbulence manipulators. It has been found that the most important feature of the wind barrier in wind protection is its porosity (Dong *et al*. 2007). Currently, porous wind barriers are being used for wind protection applications of ground vehicles in crosswind conditions.

A number of earlier papers experimentally and numerically investigated the flow behind porous

∗Corresponding author, Ph.D., E-mail: marijo.telenta@lecad.fs.uni-lj.si

http://www.techno-press.org/?journal=was&subpage=8 ISSN: 1226-6116 (Print), 1598-6225 (Online)

barriers. The experimental studies examined numerous barrier porosities, ranging from 0% to 50% porosity. The Bradley-Mulhearn experiment by Bradley and Mulhearn (1983) gave detailed measurements from full-scale field trials for a 50% porous barrier. Detailed velocity and turbulent fields behind a porous fence were measured using particle tracking velocimetry (PTV) in Lee and Kim (1999). (Dong *et al*. 2007) used a similar measuring method, that is particle image velocimetry (PIV). The Reynolds number was approximately $R_e = 1 \times 10^4$ for both measurements. Also, in previous work artificial wind barriers made of nets were analyzed. In particular, pressure drop through the screens was expressed by the wire diameter size in Wakeland and Keolian (2003). Woven windscreens with 32% porosity made of polyester were used as a scale model for canopy of trees in work ofVan Renterghem and Botteldooren (2002).

Computational Fluid Dynamic (CFD) simulation software is used to obtain insight into the flow mechanisms that contribute to the aerodynamic forces and moments acting on the vehicle. Current state-of-the-art of the aerodynamic CFD simulation process consists of CAD model creation, mesh generation, solver set-up, and solver calculation of the flow structures. Drag and lift forces, flow pathlines, and pressure distribution are extracted from the numerical solution. One of the objectives of the CFD analysis is to find the shape parameter combination to achieve optimum goal. Consequently, a large design space with numerous shape arrangements needs to be evaluated. The aerodynamics optimization simulation process, if not automated, would require significant time and effort. The paper Khondge and Sovani (2012) reports a process in which a large set of design alternatives are considered. The process combines morphing, advanced CFD solver, high performance computing, and process automaters. This methodology is used for parametric numerical simulation of barrier shelter in the current work.

Previous studies modeled fluid flow through porous geometries while not considering the details of the barrier's geometry. The main focus was to define a suitable resistance model for a given geometry of a barrier. Previous work, Packwood (2000), Fang and Wang (1997), and (Huang *et al*. 2012), used Reynolds averaging method with turbulence closure for a two-dimensional fluid flow simulation in which the porous barrier was represented as a momentum sink. As stated in Bourdin and Wilson (2008) numerical methods utilizing the momentum sink approach for wind barrier modeling treat complex unresolved flow near and through the gaps at a superficial level. A deeper understanding of the turbulent structure dynamics is required to evaluate the barrier sheltering effect. Author's previous work (Telenta *et al.* 2014) addressed this issue. URANS numerical simulations, verified with experimental data, were done in which fluid flow was simulated through geometrically accurate three-dimensional barrier model in order to resolve the flow near and through the porous barrier. The objective was to investigate the interaction between the bleed flow and the reverse flow for different barrier configurations. Present paper extends the research scope with parametric study of the bar angle influence on the barrier shelter.

Parametric numerical study in this work combines the mesh morphing and design of the experiments in automated method without re-meshing. Mesh morphing is emerging as a meaningful approach for the definition of a shape parametric CFD model. New shapes are generated by deforming the mesh of the baseline CFD model, i.e., just updating nodal positions, which requires a negligible computational time compared to any re-meshing procedure. Importantly, preserving the same mesh structure eliminates the re-meshing noise that can be confused with the effect of the design parameters.

Several algorithms have been explored for this task. A common and well-established technique, the Free Form Deformation (FFD) by Sederberg and Parry (1986) method, deforms volumes and controls their shape using a trivariate Bernstein polynomial. The method is mesh-less, so it can be

easily implemented in parallel partitioned meshes with hybrid elements. It allows the definition of new interesting shapes but it lacks accurate local surface control. Such accurate control can be achieved using mesh-based methods, for example in the pseudo-solid method (Masud *et al*. 2007), where an elastic FEM solution is used to propagate the deformation inside. Parallel implementations can in this case be difficult and extra effort is required when surface movements are not known in advance. The meeting point between these two approaches can be achieved using Radial Basis Functions (RBF) interpolation that combines the benefits of a mesh-less method with great precision. In this case the RBF morphing field is interpolated using a cloud of points with given displacements. Even if there is interesting research demonstrating that RBF can be successfully adopted for the deformation of CFD meshes, (de Boer *et al*. 2007), their numerical cost has limited their application in the past (direct solution grows by N^3 where N is the number of RBF centres). Recent efforts have been devoted to the acceleration of the method to deal with large RBF dataset. Rendall and Allen (2009, 2010) implemented and then optimized a greedy procedure so that the desired accuracy can be achieved retaining only a small subset of the original RBF cloud, demonstrating their methods for the problem of updating CFD mesh according to high order structural modes predicted using FEA. (Estruch *et al.* 2012) proposed a parallel implementation tested to deal with large meshes.

The first industrial implementation of RBF mesh morphing was introduced in 2009 with the software RBF Morph (Biancolini *et al.* 2009) that comes with a fast RBF solver for the bi-harmonic kernel which performances scales as $N^{1.6}$. A complete description of the tool is given in Biancolini (2012) while examples of applications can be found in Cella and Biancolini (2012) and Khondge and Sovani (2012).

Influence of the each bar of the wind barrier on the barrier's shelter is analyzed in the parametric study. In addition to the parametric numerical study, experimental measurement of aerodynamic forces acting on a vehicle is performed in order to document the case scenario of wind disturbance found on the motorway.

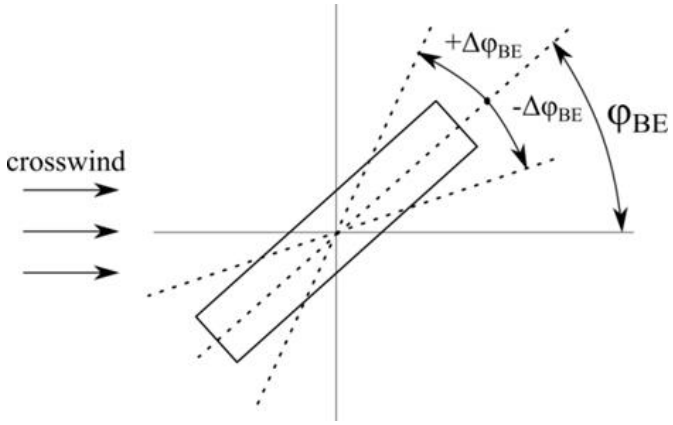

Fig. 1 Baseline bar inclination angle with a positive and negative angle increase direction

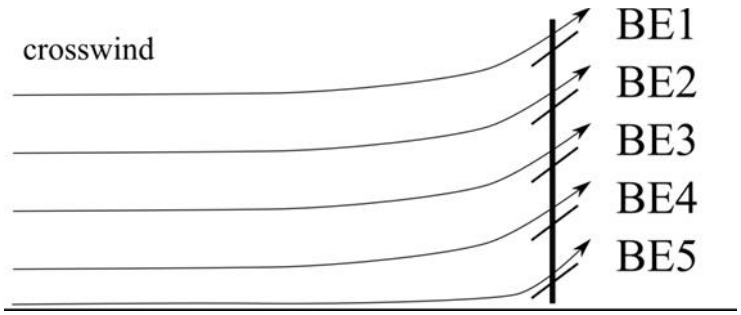

Fig. 2 Barrier configuration with the baseline parameterized bar inclination angles

1.1 Barrier model parameterization

A barrier configuration with a baseline bar inclination angle is defined. The baseline bar inclination angle, seen in Fig. 1, is set $\varphi_{BE} = 45°$ relative to the horizontal axis. The bar inclination angle is parameterized for each bar. There are five bars and, therefore, five parameters, BE1–BE5, as seen in Fig. 2. A shape morpher is utilized to change the bar inclination angle and, consequently, the volume mesh. Each bar is rotated $\Delta\varphi_{BE} = [-15°..15°]$ from the baseline angle except for the bar next to the ground which is rotated $\Delta\varphi_{BE5} = [-15°..7°]$. These limitations come from the mesh quality constraints. Design of Experiments (DOE) techniques are used to create a design point matrix over the design space to be explored. Each design point is defined by a unique combination of all defined parameter values. Aerodynamic simulation is conducted for each design point. All the data obtained from the simulation is organized and processed to generate response surface, sensitivity analysis, parallel coordinate plots and goal driven optimization studies. The morphing is performed by RBF morph software Biancolini (2012), which offers state-of-the-art scientific research to the top-level industrial requirements.

2. Experimental measurements

Experimental measurements are performed on the highway section Podnanos–Ajdovšina–Razdrto–Ajdovšina. Vehicle behavior under the influence of strong crosswind was measured and analyzed. In addition, wind velocity change with respect to time is recorded for that section of the highway. The aim of the experiment is to understand the wind conditions in which vehicles are subjected to and its effect on the vehicle's safety. Different wind conditions are documented on a section of a public road and various scenarios are defined where the wind velocity influences on the vehicle's safety without the barrier presence. These scenarios are then used in defining the boundary conditions concerning the wind profile in the numerical simulation.

The vehicle used in the experiment is a semi-trailer truck, MB Actros 1846 XL, year of manufacture 2005. The semi-trailer is Berger with three axles. The distance from the middle of the first front axle to the middle of the driven rear axle of the truck is 3.6 m and the axle distance for the semi-trailer is 1.31 m. The total length of the vehicle is 16 m, the height and the width are 4 m and 2.5 m, respectively. The front axle of the truck weighs 5400 kg, the back-axle weighs 3100 kg,

and the three axles of the semi-trailer are 1700 kg, 1700 kg, and 1800 kg. The total weight of the truck is 13232 kg. The center of gravity is at 4.9 m from the front truck axle and the ground clearance is 0.3 m.

There were six vehicle runs in total. The first run was with an intended vehicle velocity of 60 km/h, the second run was with an intended vehicle velocity of 80 km/h, and the third run was with an intended vehicle velocity of 60 km/h. Each run was performed twice, in both directions. The difference between the intended and the actual vehicle velocity is due to the conditions on the road at the time of the measurements since the experiments are done on a public road section. Details of each run, alongside the approximated force on the vehicle, are given in Table 1. Vehicle path-deviationoccurs when the vehicle under the influence of the crosswind significantly changes the pre-defined vehicle path. Figs. 3 and 4 show the measuring equipment used in the experiment. The approximated force is calculated by Eq. (1).

$$F = \frac{1}{2}\rho u_R^2 c_x A \tag{1}$$

where A is the vehicle side area, u_R is the resultant velocity, c_x =1.15 is the resistance coefficient Roy and Srinivasan(2000), and ρ is the air density.

Table 1 Vehicle path-deviation occurrences with approximated force on the vehicle

Run	Vehicle path-deviation occurrences	Vehicle velocity (km/h)	Maximal wind velocity (km/h)	Approximated force on the full scale vehicle (N)
1	0	42	121	57 063
2	0	61	108	53 515
3	**7**	**79**	**178**	**131 918**
4	1	55	139	77 728
5	0	50	117	56 312
6	1	59	112	55 741

Fig. 3 Data collection (Batista 2011)

Fig. 4 3-D anemometers (Batista 2011)

Fig. 5 Vehicle path deviations (m) for vehicle run 3 (Batista 2011)

One can see from Tab.1 that vehicle run 3 has the most vehicle path deviations, Fig. 5. Hence, this scenario was taken for wind barrier implementation in numerical simulation. In addition, Table 1 shows scenarios where no vehicle path deviation occurs, in particular, runs 1 and 2. The approximated force from the run 1 is taken as the maximum force on the vehicle at which there is no vehicle path deviation.

3. Computational method

An aerodynamic goal driven simulation process needs to be accurate, extensive and automated. To insure accuracy, 23 million hexahedral mesh elements are generated for the numerical simulation. In addition, the design space is represented by 55 design points in order for the optimization to be extensive. Finally, Ansys Workbench is used as an automation platform. The

goal is to present a parametric aerodynamic simulation methodology that can be implemented for wind barrier simulation with accuracy and an extended design space in an automated manner.

3.1 RBF Morph

The mesh morpher modifies the mesh via small shape modifications without changing its topology. The technique uses Radial Basis Functions (RBF), Table 2. The method is based on a system of radial functions for mesh movement, namely morphing. The RBF Morph software is fully integrated with Ansys Fluent and offers user-friendly interaction within the Fluent working environment. The shape changes can be parameterized and, thus, parametric studies can be performed. The basic function of the morpher is to change the location of the nodes of the mesh elements. This allows changing the barrier configuration without re-meshing the model. The morpher changes the object shape and subsequently morphs the volume mesh around the object.

3.2 CFD setup and parameterization

A volume hexahedral mesh was generated for the baseline model, as seen in Fig. 6. It consists of 23 million elements. Values of y^+ are set low (below 1) near the ground, the barrier and the vehicle surfaces. Refinement zones are created in critical areas such as separations and wakes. This is sufficient for accurate numerical simulation. Boundary conditions, mesh size, models, and solver settings used are in accordance to the aerodynamics simulation best practices from the author's prior work. The numerical approach has been validated using wind tunnel measurements involving wind barrier in author's previous work (Telenta *et al.* 2013) and (Telenta *et al.* 2014)and the present parametric aerodynamic simulation is focused on a practical application.

Table 2 Typical radial basis functions

Radial Basis Function	$\phi(r)$
Spline type (R_n)	$\lvert r\rvert^n$, n odd
Thin plate spline (TPSn)	$\lvert r\rvert^n \log\lvert r\rvert$, n even
Multiquadratic (MQ)	$\sqrt{1+r^2}$
Inverse multiquadratic (IMQ)	$1/\sqrt{1+r^2}$
Inverse quadratic (IQ)	$1/\left(1+r^2\right)$
Gaussian (GS)	e^{-r^2}

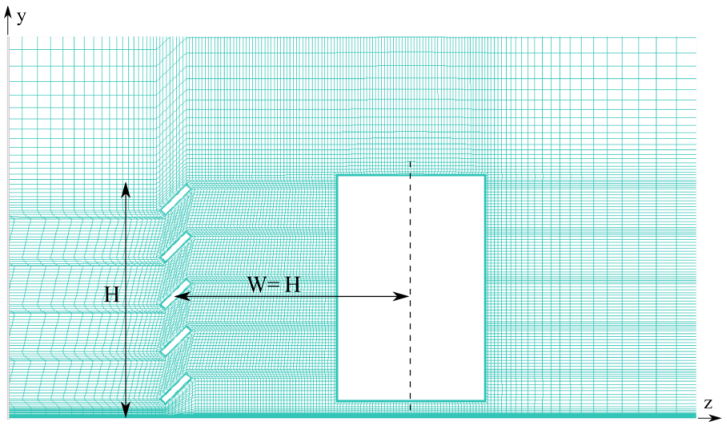

Fig. 6 Hexahedral mesh for baseline barrier configuration

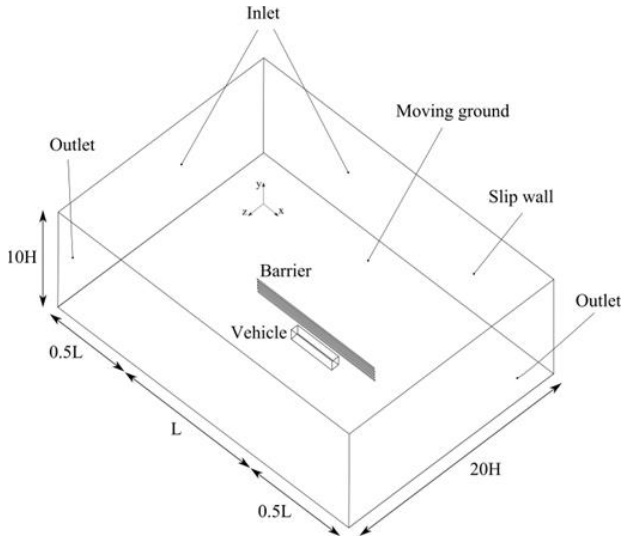

Fig. 7 Computational domain

3.3 Numerical simulation setup

Three-dimensional RANS numerical simulation was utilized. A commercial CFD code, Ansys Fluent 14.5, was used to solve the equations of fluid motion. A crosswind scenario was considered in the numerical simulation. Therefore, the computational domain, as seen in Fig. 7, consists of two inlets and two outlets. The top side of the domain is modeled as symmetry. The ground, barrier and vehicle surfaces are modeled as no-slip walls. The constant velocity inlet was set with two velocity components, a streamwise component with 22 m/s and a sidewise component with 50 m/s. These are the highest velocity values measured in the experiment and represent the most critical vehicle crosswind scenario. The velocity data were taken from the experimental measurements Batista (2011). The outlet is modeled as a constant static pressure outlet with zero gage pressure. A

moving wall with 22 m/s streamwise velocity was set for the ground and the barrier surfaces, whereas a stationary wall was set for the vehicle surface. A moving mesh was avoided with this boundary configuration. The barrier model length L and height H are $4.56\,\mathrm{m}$ and $0.4\,m$, respectively, Fig. 6. The numerical domain size is chosen in order to correspond to the open field measurements. The domain width, height, and length are $20 \times \mathrm{H}$, $10 \times \mathrm{H}$, $2.5 \times \mathrm{L}$, respectively.The domain size is selected following the recommendations from the previous work by Bourdin and Wilson (2008). The vehicle is positioned relatively to the barrier to be fully involved in the barrier's wake. In particular, the distance between the front end of the barrier and the front end of the vehicle is $1.25 \times \mathrm{L}$. The vehicle is fully sheltered by the barrier considering the crosswind angle and the vehicle's relative position to the barrier. The corresponding Reynolds number is $R_e = 14.56 \times 10^5$. The aerodynamic coefficients are assumed to be equal for the full-scale vehicle because the Reynolds number is higher than the critical Reynolds number where the separation is fully turbulent. No wall functions were used for boundary layer modeling. The pressure based coupled solver was used with Green gauss node-based gradients. The accuracy of the numerical simulation for turbulent flow depends on the fidelity of the turbulence model. This is particularly important if flow exhibits strong separation and vortices. Therefore, the SST $k-\omega$ turbulence model was used. The second-order accurate central discretization for the diffusion terms, the second-order accurate upwind discretization for the advection terms, and the second-order accurate time discretization were used. The standard algorithm was applied for pressure-velocity coupling. The CFD solver was run for 2250 iterations for each design point. Computations were calculated until the maximum continuity residual dropped five orders of magnitude. Also, integral value, the barrier drag, was monitored during the numerical procedure. The convergence of the numerical simulation was achieved when the barrier drag became statistically steady.

3.4 Governing equations

Fluid flow is described by incompressible Navier-Stokes equations

$$\frac{\partial u_i}{\partial t} + u_j \frac{\partial u_i}{\partial x_i} = -\frac{1}{\rho}\frac{\partial p}{\partial x_i} + \nu \nabla^2 u_i, \; i=1,2,3 \tag{2}$$

$$\frac{\partial u_i}{\partial x_i} = 0 \tag{3}$$

where u_i is the i-component of the velocity, x_i is the i-direction, t is the time, p is the pressure, ρ is the density and v is the kinematic viscosity. Eq. (2) represents the momentum equations, and Eq. (3) represents the continuity equation.

3.5 Turbulence modeling

The governing equations due to the Reynolds averaging procedure have additional unknown variables, known as Reynolds stresses. Thus, the governing equations need a turbulence model to be solved. The turbulence model used is the shear stress transport (SST) k-ω. The k-ω model is a two-equation eddy-viscosity model where the Reynolds stresses are linearly related to the mean velocity gradient (Boussinesq hypothesis) through an eddy-viscosity coefficient. Two additional

transport equations have to be solved, one for the kinetic energy and one for the dissipation per unit turbulence kinetic energy, to compute the local values of the eddy viscosity. The k-ω model is more accurate then k-ε model in the near wall layers, but it fails for flows with pressure induced separation. In addition, ω equation shows strong sensitivity to the values of ω in the free-stream outside the boundary layer. This was the motivation for the development of SST models.

3.5.1 SST k-ω turbulence model

The SST k-ω turbulence model is a two-equation eddy-viscosity model. The main problem with the Wilcox k-ω model is its strong sensitivity to free-steam conditions. To overcome this, Menter (1994) developed a model to combine the k-ω model near the surface and the k-ε model in the outer region. However, this model still fails to properly predict the onset and amount of flow separation from smooth surfaces. The main reason is that the model does not account for the transport of the turbulent shear stress. This results in an over-prediction of the eddy-viscosity.

SST model formulation (Menter *et al.* 2003)

$$\frac{\partial(\rho k)}{\partial t}+\frac{\partial(\rho u_i k)}{\partial x_i}=\tilde{P}_k-\beta^*\rho k\omega+\frac{\partial}{\partial x_i}\left[(\mu+\sigma_k\mu_t)\right]\frac{\partial k}{\partial x_i}\frac{\partial \omega}{\partial x_i} \tag{4}$$

$$\frac{\partial(\rho\omega)}{\partial t}+\frac{\partial(\rho u_i k)}{\partial x_i}=\alpha\rho S^2-\beta\rho\omega^2+\frac{\partial}{\partial x_i}\left[(\mu+\sigma_\omega\mu_t)\frac{\partial\omega}{\partial x_i}\right]+2(1-F_1)\rho\sigma_{\omega 2}\frac{1}{\omega}\frac{\partial k}{\partial x_i}\frac{\partial\omega}{\partial x_i} \tag{5}$$

where blending function F_1 is defined

$$F_1=\tanh\left\{\left\{\min\left[\max\left(\frac{\sqrt{k}}{\beta^*\omega y},\frac{500\nu}{y^2\omega}\right),\frac{4\rho\sigma_{\omega 2}k}{CD_{k\omega}y^2}\right]\right\}^4\right\} \tag{6}$$

with

$$CD_{k\omega}=\max\left(2\rho\sigma_{\omega^2}\frac{1}{\omega}\frac{\partial k}{\partial x_i}\frac{\partial\omega}{\partial x_i},10^{-10}\right)$$

and y is the distance near the wall.

F_1 is equal to zero away from the surface (k-ε model), and switches over to one inside the boundary layer (k-ω model).

The turbulent eddy viscosity is defined

$$\nu_t=\frac{a_1 k}{\max(a_1\omega,SF_2)} \tag{7}$$

where k is the turbulence kinetic energy, ω is the turbulent frequency, F_2 is a blending function, S is an invariant measure of the strain rate, and a_1 is a coefficient.

$$F_2=\tanh\left[\left[\max\left(\frac{2\sqrt{k}}{\beta^*\omega y},\frac{500\nu}{y^2\omega}\right)\right]^2\right] \tag{8}$$

Production limiter is used in the SST model to prevent the build-up of turbulence in stagnation region

$$P_k = \mu_t \frac{\partial u_i}{\partial x_j}\left(\frac{\partial u_i}{\partial x_j} + \frac{\partial u_j}{\partial x_i}\right) \tag{9}$$

$\tilde{P}_k = \min\left(P_k, 10 \cdot \beta^* \rho k\omega\right)$

All constants are computed by a blend from the corresponding constants of the k-ε and the k-ω model via $\alpha_1 = \alpha_1 F + \alpha_2(1-F)$.

The constants are $\beta^* = 0.09$, $\alpha_1 = 5/9$, $\beta_1 = 3/40$, $\sigma_{k1} = 0.85$, $\sigma_{\omega 1} = 0.5$, $\alpha_2 = 0.44$, $\beta_2 = 0.0828$, $\sigma_{k2} = 1, \sigma_{\omega 1} = 0.856$.

The vehicle model is represented by a simple box, with a 1:10 ratio to the full size model used in the experimental investigation. The vehicle model height and length are 0.38 m and 1.6 m, respectively. The simple shape of the vehicle model was used to lower the geometric complexity and, thus, numerical difficulty for the turbulence model.

3.6 Design space creation

Parameters and optimization method are important features for design optimization study. In particular, parameters form the design space basis. Design points are defined using the DOE technique to accurately represent the entire design space. Performance data, such as aerodynamic force, is calculated for each design point. The design points, together with the performance data, are analyzed to understand the effect of the parameters on the aerodynamic forces and seek the optimum design.

Five parameters, one for each bar, are considered. The parameters define the bar position. The angle is measured with reference to the baseline model, as seen in Fig. 1. The net design space is bounded by the maximum and minimum values of the five parameters.

The design of the experiments represents a procedure that determines the optimum design points within a given design space. The goal of the DOE schemes is to identify a set of sampling points such that the entire design space is efficiently explored with a minimum number of sampling points. The DOE matrix was generated with the Central Composite Design (CCD) scheme with the enhanced face centered option. The CCD scheme gives homogenous coverage of the design space. The CCD scheme generated 55 design points for the five parameters. After completion of the numerical simulation for all design points, the DOE table is populated with input variables and output solver parameters. Response surfaces for the side force versus the five input parameters are created. Several different algorithms are available for generating response surfaces. In this work, the non-parametric regression (NPR) algorithm is implemented for predictably high nonlinear relation between outputs and inputs. Because there are five parameters, the side force response surface represents a surface in six-dimensional space, which is difficult to represent. Instead, two-dimensional and three-dimensional graphs are generated. The two-dimensional graph shows the variation of the side force with respect to one parameter, with the other four parameters held constant. The three-dimensional graph shows the variation of the side force with respect to two parameters, and the other parameters are being held constant at a fixed value.

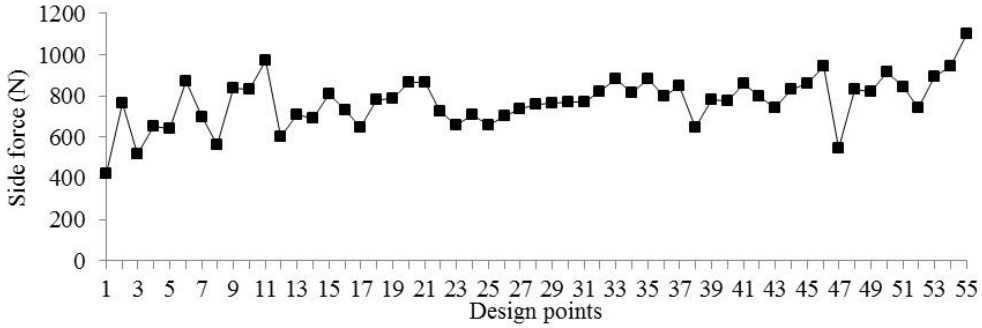

Fig. 8 Side force vs. design points

4. Results

The bar inclination angle is set as input data and the vehicle side force is set as output data. Response surfaces are created using the input and the output data. Optimization studies are conducted with the response surfaces, which are also visualized. A non-parametric method is used for preparation of the response surfaces.

Five parameters for the bar inclination angle, $\Delta\varphi_{BE1}$–$\Delta\varphi_{BE5}$, for a given data range and the resulting vehicle side force, N, are analyzed. Fig. 8 shows the variation of the side force versus the design points, whereas Fig. 10 shows the variation of the side force versus the parameters.

Fig. 9 shows the goodness of the plot fit for the response surface generated for the test case. The vehicle side force calculated from the CFD simulations is represented on the horizontal axis, while the vehicle side force predicted by the response surface is represented on the vertical axis. Points shown in the plot represent the design points. The solid line represents the ideal response surface with no error. One can see from Fig. 9 that the response surface is highly accurate.

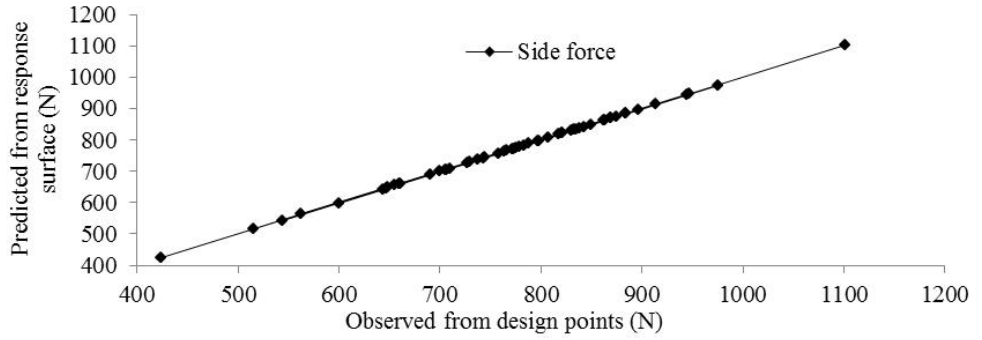

Fig. 9 Goodness of the fit of the response surface

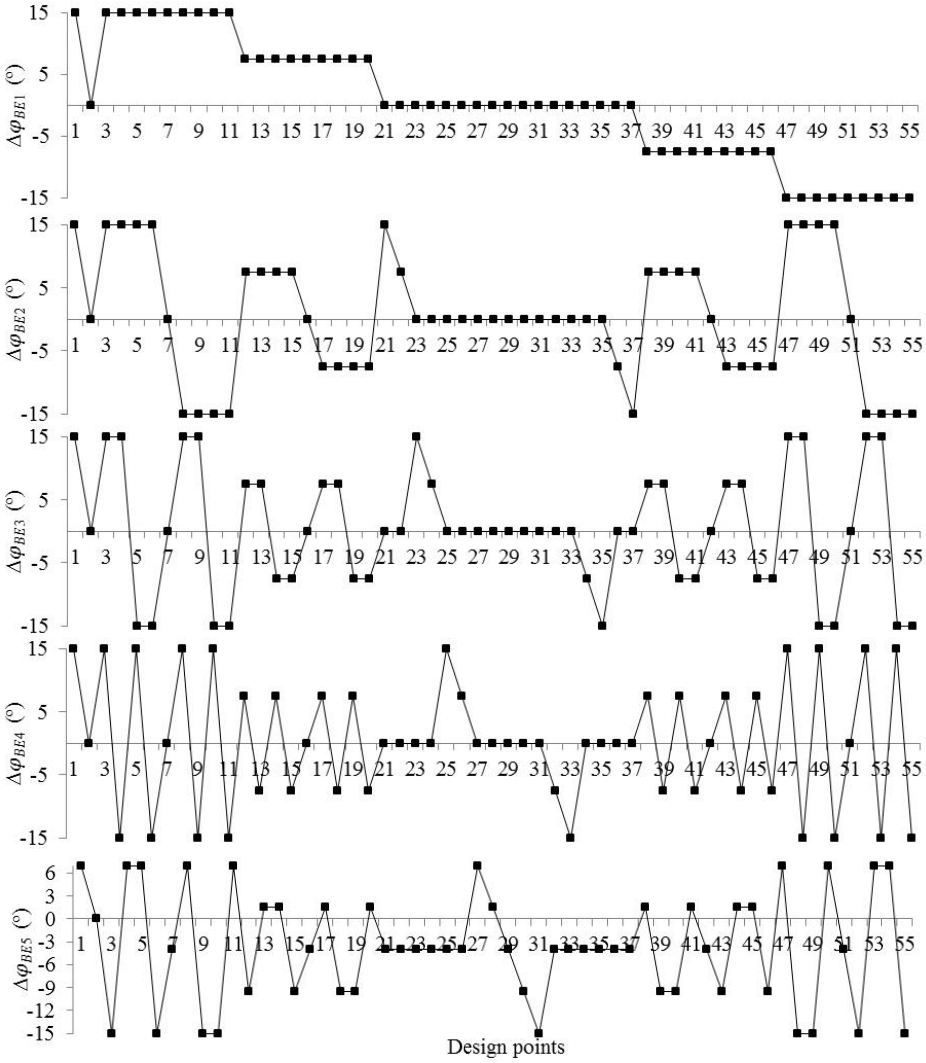

Fig. 10 Design points vs. parameters

4.1 Sensitivity study and trade-off analysis

Fig. 11 shows the two-dimensional response surface that presents the variation of the vehicle side force with respect to one parameter while all other parameters are held constant. Fig. 12 shows the three-dimensional response surface where variations of the vehicle side force with respect to two parameters are presented. One can see from Fig. 11 that the trend is similar for all parameters except the last one.

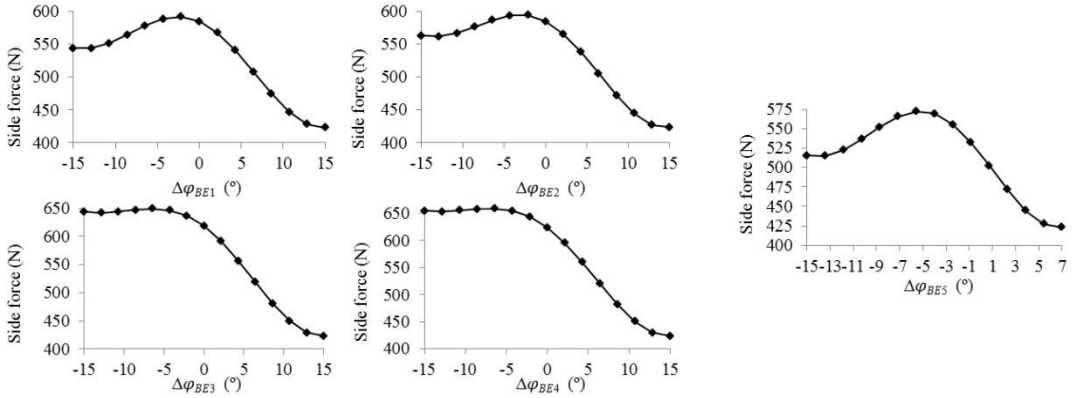

Fig. 11 Two-dimensional response surfaces

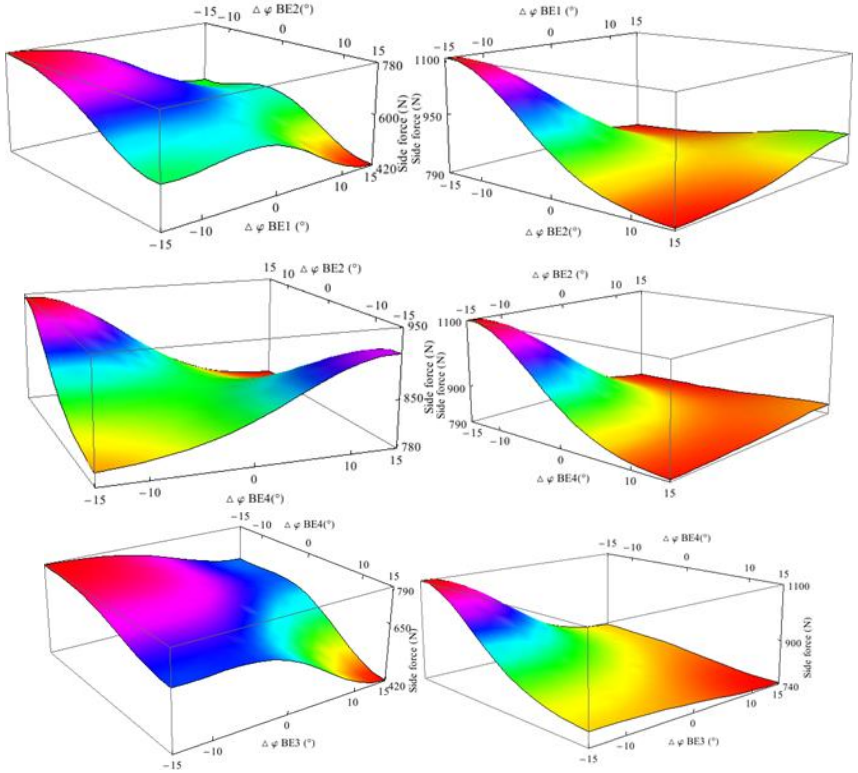

Fig. 12 Three-dimensional response surfaces

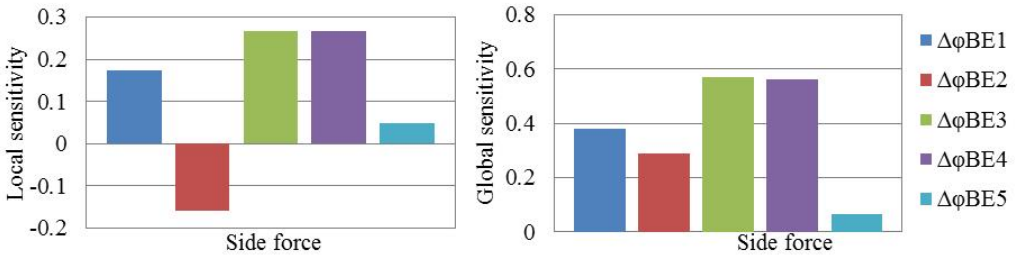

Fig. 13 Local and global sensitivity chart of the side force

The local sensitivity chart represents the side force sensitivity to the parameters at a particular design point. Fig. 13 shows the local sensitivity of the side force for the baseline design point. One can see from Fig. 13 that the largest influences on side force have the $\Delta\varphi_{BE3}$ and the $\Delta\varphi_{BE4}$ parameters. The smallest impact has the $\Delta\varphi_{BE5}$ parameter. Global sensitivity represents the average side force sensitivity to each parameter averaged over all design points in the entire design space, as seen in Fig. 13. Again, the largest influences on the side force have $\Delta\varphi_{BE3}$ and $\Delta\varphi_{BE4}$.

4.2 Optimization study

The wind barrier application goal is to lower the aerodynamic forces on the sheltered vehicle. One can see from Table 3 the design point that gives the minimum vehicle side force. However, other requirements need to be satisfied along with the reduction of the vehicle's aerodynamic forces. These requirements include reduction of the aerodynamic forces on the barrier. Larger barrier porosity implies smaller aerodynamic forces on the barrier. Larger barrier porosity is achieved when the bar inclination angles are maximized.

Parametric study is used as a quick research of the parameters influence on the barrier and vehicle force values. In addition to the minimum vehicle side force objective, other objectives are set to be satisfied. Hence, goal driven optimization is conducted, where two of the most influential parameters values are set to maximum and other parameters are minimized. Fig. 13 shows that two parameters, $\Delta\varphi_{BE3}$ and $\Delta\varphi_{BE4}$, have the biggest influence on the side force value. Therefore, a goal driven study is conducted where $\Delta\varphi_{BE3}$ and $\Delta\varphi_{BE4}$ parameters are set to be maximized and other parameters are set to be minimized. Table 4 lists three barrier configurations with their calculated vehicle side force value, along with the corresponding bar angles. As a result of the goal driven study, configuration C was defined. As one can see from Table 4, only configuration A has an acceptable side force value on the vehicle for which there is no vehicle path deviation. The velocity contours for the three barrier configurations are shown in Fig. 14.

Table 3 Minimum, maximum and goal driven optimization vehicle side force values

Barrier configuration	φ_{BE1} (°)	φ_{BE2} (°)	φ_{BE3} (°)	φ_{BE4} (°)	φ_{BE5} (°)	Side force on the vehicle model (N)
A	60	60	60	60	52	423.34
B	30	30	30	30	30	1096.79
C	30	30	59	58	31	749.6

Table 4 Side force on the full-scale vehicle for the three barrier configurations

Barrier configuration	Side force on the full-scale vehicle for the run 3 scenario (N)	Approximated side force on the vehicle for the run 3 scenario (N)
Configuration A	42 334	131 918
Configuration C	74 960	Approximated side force on the vehicle for the scenario with no vehicle path deviation (N)
Configuration B	109 679	57 063

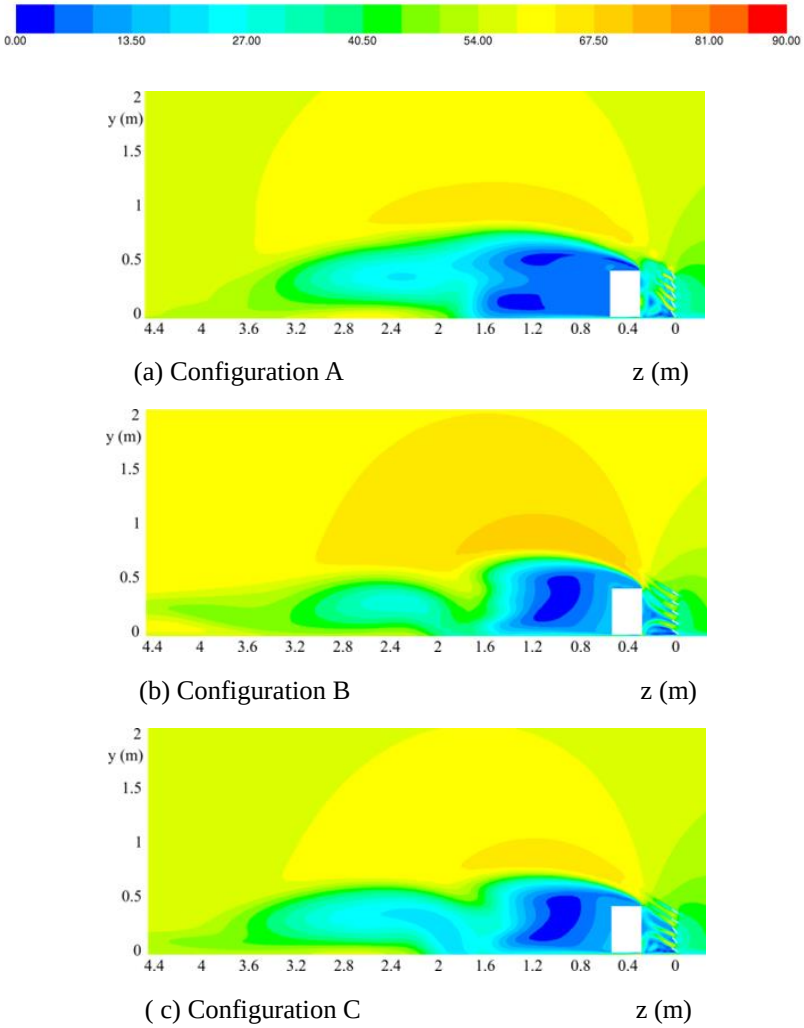

(a) Configuration A

(b) Configuration B

(c) Configuration C

Fig. 14 Velocity profile for three barrier configurations (m/s)

Table 5 Side force distribution on each bar per vehicle length for the three barrier configurations

Force (N)	Barrier configuration A full scale	Barrier configuration B full scale	Barrier configuration C full scale
BE1	18 642	7 993	8 099
BE2	23 963	9 781	9 913
BE3	26 796	11 057	17 974
BE4	27 626	12 141	21 434
BE5	18 331	10 517	12 088
Total	115 358	51 489	69 508

The geometric porosity of the barrier is defined as the ratio of the total open area between the bars and the total area occupied by the barrier. As the barrier bar angle changes, the barrier's porosity follows that change. Lower bar angle value yields higher barrier porosity and smaller shelter protection. Hence, barrier configuration A has the smallest porosity and highest wind protection whereas barrier configuration B has the smallest porosity and consequently smallest wind protection. Barrier porosity for the configuration A is 35% porosity, whereas for the barrier configuration B the porosity is 62.5%. Barrier configuration C has 51.5% porosity.

Table 5 shows the side force per barrier length distribution on each bar for the three barrier configurations. One can see that the force distribution is essentially uniform considering each bar for the barrier configurations A and B, whereas for the barrier configuration C, the BE3 and BE4 bars have much larger side force values than the rest of the bars.

5. Conclusions

Parametric numerical study was conducted for the wind barrier configuration. The wind barrier consists of five bars and was accurately geometrically represented by a three-dimensional model. RANS numerical simulation was utilized with the SST $k-\omega$ turbulence model. Boundary conditions, mesh size, models, and solver settings used in the numerical simulation are in accordance to the aerodynamics simulation best practices from the author's prior work. Parametric numerical study in this work combines the mesh morphing and design of the experiments in automated manner. The wind barrier optimization method consists of mesh morphing, an advanced CFD solver, high performance computing, and process automaters. The baseline barrier configuration was set with a 45° bar inclination angle. Each bar is rotated $\Delta\varphi_{BE} = [-15°..15°]$ from the baseline angle except for the bar next to the ground which is rotated $\Delta\varphi_{BE5} = [-15°..7°]$. The design space for aerodynamic optimization was represented by 55 design points. In addition, experimental measurement of aerodynamic loads acting on the vehicle is done. The goal of this work is to present a parametric aerodynamic simulation methodology for the wind barrier that integrates accuracy and an extended design space in an automated manner.

The primary goal of the study was to define a barrier configuration that provides the smallest vehicle side force value. This is achieved with the barrier configuration A. However, other aspects

of the barrier application can be considered besides the minimum vehicle side force goal. Sensitivity study gives the most influential parameters for the side force on the vehicle. Hence, goal driven optimization is conducted, where the two of the most influential parameters are set to their maximum and the other parameters are minimized. Barrier configuration C represents the outcome of the goal driven optimization. However, with this goal optimization, the vehicle side force was increased above the value for which vehicle path deviations occur. Automated parametric numerical study is essential in order to find the optimal barrier configuration.

References

Batista, M. (2011), *Meritev obnašanja tovarnega vozila pri močni burji na cestnem odseku hitre ceste Razdrto-Vipava-Ajdovščin,* Portorož, Slovenia.

Biancolini, M.E. (2012), "Mesh morphing and smoothing by means of radial basis functions (RBF): a practical example using Fluent and RBF Morph", *Handbook of Research on Computational Science and Engineering*, 347-380.

Biancolini, M., Biancolini, C., Costa, E.G.D. and Valentini, P. (2009), "Industrial application of the meshless morpher RBF morph to a motorbike windshield optimisation", *Proceedings of The European Automotive Simulation Conference*, Munich.

Biancolini, M., Viola, I. and Riotte, M. (2014), "Sails trim optimisation using CFD and RBF mesh morphing", *Comput Fluids*, **93**, 46-60.

Bourdin, P., and Wilson, J. D. (2008), "Windbreak aerodynamics: is computational fluid dynamics reliable? ", *Bound. - Lay. Meteorol.*, **126**(2), 181-208.

Bradley, E. and Mulhearn, P. (1983), "Development of velocity and shear stress distributions in the wake of a porous shelter fence", *J. Wind Eng. Ind. Aerod*., **15**(1-3), 145-156.

Cella, U.B. and Biancolini, M. (2012), "Aeroelastic analysis of aircraft wind-tunnel model coupling structural and fluid dynamic codes", *J. Aircraft*, **49**(2), 407-414.

de Boer, A., van der Schoot, M. and Bijl, H. (2007), "Mesh deformation based on radial basis function interpolation", *Comput Struct.*, **85**(11-14), 784-795.

Dong, Z., Luo, W., Qian, G. and Wang, H. (2007), "A wind tunnel simulation of the mean velocity fields behind upright porous fence", *Agric. For. Meterol*., **146**(1-2), 82-93.

Estruch, O., Lehmkuhl, O., Borrell, R., Pérez Segarra, C. and Oliva, A. (2012), "A parallel radial basis function interpolation method for unstructured dynamic meshes", *Comput Fluids*, **10**, 44-54.

Fang, F.M. and Wang, D.Y. (1997), "On the flow around a vertical porous fence", *J. Wind Eng. Ind. Aerod*., **67-68**, 415-424.

Huang, L.M., Chan, H.C. and Lee, J.T. (2012), "A numerical study on flow around nonuniform porous fences", *J. Appl. Math*., **2012**.

Khondge, A. and Sovani, S. (2012), *An accurate, extensive, and rapid method for aerodynamics optimization: The 50:50:50 Method*, *SAE Technical Paper*.

Lee, S.J. and Kim, H.B. (1999), "Laboratory measurements of velocity and turbulence field behind porous fences", *J. Wind Eng. Ind. Aerod.*, **80**(3), 311-326.

Masud, A., Bhanabhagvanwala, M. and Khurram, R.A. (2007), "An adaptive mesh rezoning scheme for moving boundary flows and fluid–structure interaction", *Comput Fluids*, **36**(1), 77-91.

Menter, F.R. (1994), "Two-equation eddy-viscosity turbulence models for engineering applications", *AIAA J*., **32**(8), 1598-1605.

Menter, F.R., Kuntz, M. and Langtry, R. (2003), *Ten years of industrial experience with the SST turbulence model*,Turbulence, Heat and Mass Transfer.

Packwood, A. (2000), "Flow through porous fences in thick boundary layers: comparisons between laboratory and numerical experiments", *J. Wind Eng. Ind. Aerod*., **88**(1), 75-90.

Rendall, T. and Allen, C. (2009), "Efficient mesh motion using radial basis functions with data reduction algorithms", *J. Comput. Phys.*, **228**(17), 6231-6249.
Rendall, T. and Allen, C. (2010), "Reduced surface point selection options for efficient mesh deformation using radial basis functions", *J. Comput. Phys.*, **229**(8), 2810-2820.
Roy, S. and Srinivasan. (2000), *External flow analysis of a truck for drag reduction*, *SAE*.
Sederberg, T.W.P. and Parry, S.R. (1986), "Free-form deformation of solid geometric models", *Proceedings of the 13th Annual Conference on Computer Graphics and Interactive Techniques (SIGGRAPH '86)*, 151-160. New York, (Eds., D.C. Evans and R.J. Athay). ACM.
Telenta, M., Duhovnik, J., Kosel, F. and Šajn, V. (2013), "Wake interaction of a rectangular prism behind a geometrically accurate porous barrier", *Technical Gazette*, **20**(5), 877-882.
Telenta, M., Duhovnik, J., Kosel, F. and Šajn, V. (2014), "Numerical and experimental study of the flow through a geometrically accurate porous wind barrier model", *J. Wind Eng. Ind. Aerod.*, **124**, 99-108.
Van Renterghem, T. and Botteldooren, D. (2002), "Reducing screen-induced refraction of noise barriers in wind by vegetative screens", *Acta Acust. United Acust*., **88**(2), 231-238.
Wakeland, R. and Keolian, R. (2003), "Measurements of resistance of individual square-mesh screens to oscillating flow at low and intermediate reynolds numbers", *J. Fluid. E*ng. - *T ASME*, **5**(125), 851-862.

CC